Electrochimica Acta 322 (2019) 134766

Contents lists available at ScienceDirect

Electrochimica Acta

journal homepage: www.elsevier.com/locate/electacta

# Thickness-dependent electrochemical response of plasma enhanced atomic layer deposited $WS_2$ anodes in Na-ion battery

Dip K. Nandi [a], Seungmin Yeo [b], Mohd Zahid Ansari [a], Soumyadeep Sinha [c], Taehoon Cheon [a, d], Jiseok Kwon [e], Hyungjun Kim [b], Jaeyeong Heo [c], Taeseup Song [e, *], Soo-Hyun Kim [a, *]

[a] *School of Materials Science and Engineering, Yeungnam University, 214-1, Dae-dong, Gyeongsan-si, 38541, Republic of Korea*
[b] *School of Electrical and Electronic Engineering, Yonsei University, Seodaemun-gu, Seoul, 03722, Republic of Korea*
[c] *Department of Materials Science and Engineering, and Optoelectronics Convergence Research Center, Chonnam National University, Gwangju, 61186, Republic of Korea*
[d] *Center for Core Research Facilities, Daegu Gyeongbuk Institute of Science & Technology, Sang-ri, Hyeonpung-myeon, Dalseong-gun, Daegu, 711-873, Republic of Korea*
[e] *Department of Energy Engineering, Hanyang University, Seoul, 133-791, Republic of Korea*

## ARTICLE INFO

*Article history:*
Received 26 April 2019
Received in revised form
19 July 2019
Accepted 26 August 2019
Available online 27 August 2019

*Keywords:*
Tungsten sulfide
Atomic layer deposition
Film thickness
Na-ion battery
Anode

## ABSTRACT

In spite of the promising future of the Sodium (Na)-ion batteries (NIBs), it still suffers with low specific capacity and stability mostly owing to the slow kinetics associated with Na ion. In this regard, transition metal sulfides (TMSs) are considered to be one of the best anode materials that can efficiently store Na ions not only owing to their graphite-like layered structure but also through conversion reactions facilitated by their multi-oxidation states. However, the poor cyclic stability of these TMSs attributed to the low electronic conductivity of the TMSs hinders the practical use. Therefore, understanding on an optimized mass loading (or physical dimensions) and configuration of such active electrode material are essential to improve the kinetics associated with Na-ion and electron pathway. To study this, plasma-enhanced atomic layer deposition (PEALD) is employed to grow $WS_2$ using tungsten hexacarbonyl $[W(CO)_6]$ and $H_2S$ plasma as a precursor and reactant, respectively. The thin films of $WS_2$ deposited directly on stainless steel coin with varying ALD cycles (200–600) are then tested as anode in NIBs without any binder or conducting carbon. Two-stage growth mode is observed with increasing number of ALD cycles which leads to $WS_2$ nano-flakes formation on top of a two-dimensional film of the same. Reversible conversion and intercalation reactions from the cyclic voltammetry measurements are evident for the electrochemical stability of these pristine-$WS_2$ films. While the highest areal capacity of ~58.8 μAh/cm$^2$ at a current density of 50 μA/cm$^2$, after 50 charge-discharge cycles, is achieved with 400 ALD cycles, the highest capacity retention (~72.5%) is observed for the film deposited with minimum (200) ALD cycles under same conditions. However, the capacity as well as its retention degrades drastically when the number of ALD cycles is further increased beyond 400. In this study, we address a critical issue associated with $WS_2$ as an anode material for NIBs which should be similarly true for other TMSs as well.

© 2019 Elsevier Ltd. All rights reserved.

## 1. Introduction

The necessity of environmentally friendly energy generations as well as energy storage devices reaches into a new height in the 21st century. In this regard, electrochemical energy storage becomes one of the most important research areas because of its huge demand in portable electronics and for the rapidly growing market of electric vehicles [1–3]. Energy storage devices mainly including rechargeable batteries and the supercapacitors are considered to meet this challenge together [4,5]. Along with several Li-based energy storage technologies (Li-ion, Li–$O_2$, Li–S batteries), Na-ion batteries (NIBs) has also gained significant attraction in past

---

* Corresponding authors.
*E-mail addresses:* tssong@hanyang.ac.kr (T. Song), soohyun@ynu.ac.kr (S.-H. Kim).

https://doi.org/10.1016/j.electacta.2019.134766
0013-4686/© 2019 Elsevier Ltd. All rights reserved.

several years [6–12]. NIBs are considered as a promising alternative to Li-ion batteries (LIBs) because of the abundance and low cost of Na [13,14]. However, several disadvantages of NIBs hinder its practical implantation, the most crucial among them being the severe capacity fading owing to the slow kinetics of sodiation during discharging of the cell [15]. Intrinsically, larger size of Na-ions compared to Li-ions leads to such slow kinetics especially in sodiation process where Na-ions are stored inside of an active material. Though the extensive studies have been carried out on different electrode materials for NIBs, there is relatively less amount of explorations on several specific aspects of the anode materials [16–20]. The focus on carbon material hinders such attempts which are slowly being shifted to other potential materials in recent time [13,14,21–24]. The major reason to find a replacement for carbon based active electrode material is the capacity limit (less than 300 mAh/g) of such anode.

On the other hand, transition metal dichalcogenides (TMDCs; $MX_2$ where M is Mo, W etc.; X is S, Se or Te) for their layered structure and versatile opto-electronic properties have drawn significant attention of research community in past several years for various applications [25–28]. Among all of such materials, $MoS_2$ and $WS_2$ are extensively explored from the application point of view and $MoS_2$ is the most widely studied anode material over the past decade in both, LIBs as well as NIBs [29–34]. Though this material has displayed extremely high specific capacity and excellent rate capability or stability, the reaction mechanism involving intercalation, conversion and elemental sulfur ($S_8$)-based reaction after first discharge cycle is yet to be fully understood [35]. On the other hand, an increasing number of attempts with other Mo and W based dichalcogenides ($MoSe_2$, $WS_2$ and $WSe_2$) as an anode in LIBs/NIBs have been made owing to their graphene (or $MoS_2$)-like layered structure [36]. However, $WS_2$ is relatively less explored compared to $MoS_2$ probably due to its lower specific capacity resulting from higher atomic weight [37–44]. The earlier reports on employing nanostructured $WS_2$ showed promising results in NIBs, however, it's large volume change during sodiation and desodiation due to the large size of Na-ion results in the drastic capacity fading for bulk/pristine $WS_2$ anode making it not to be a potential candidate for long cycling life of the battery [39,41–44]. However, $WS_2$ composites with graphene or N-doped carbon (NC) showed much better stability with enhanced capacity in NIBs by increasing the conductivity of the composite due to the presence of carbon in the electrode [39,42,43]. Interestingly, it was also reported in literature that the $WS_2$ NWs displayed higher electrochemical activity that leading to a significant increment in the capacity in NIBs compared to the bulk $WS_2$ [41]. From the earlier studies, it could be realized that the resistive nature of this material restricts the easy electron and ion transport inside pristine $WS_2$. In this regard, it is necessary to reveal the limitation of the sodiation into pristine $WS_2$ nanostructures with increasing dimensions through the fundamental study for establishing this material further as a potential candidate for NIBs anode. Therefore, it is imperative to know the response of pristine-$WS_2$ thin films in details with increasing dimensions. Nevertheless, such study is difficult for an electrode fabricated in a conventional way. This can be done in a controlled way of growth of the material. Atomic layer deposition (ALD) could be considered as the best candidate to grow the $WS_2$ thin films with desired thickness by varying the number of ALD cycles during deposition.

Though few recent works showed relatively good performance of NIBs that involved ALD but, there are still very less amount of works which could establish ALD in the field NIBs to its fullest capacity [45–48]. Because of the self-limiting nature of the reactions, the thickness of the ALD-grown films could be controlled up to few Angstrom (Å), which would be the thickness of a mono-layer of the material. There are few articles on ALD of $WS_2$ prepared using $WF_6$ as a W-source and $H_2S$ (sometime along with $H_2$ plasma) and used as a solid lubricant [49–51]. However, using $WF_6$ might restrict the applications of the film owing to the presence of corrosive F in the film as well as the generation of HF during reaction as a by-product. Recently, Matinnen et al. introduced an metal-organic precursor ($W_2(NMe_2)_6$) with $H_2S$ toward low temperature (150 °C) deposition of S-deficient amorphous $WS_2$ films [52]. In recent time, we have also carried out the plasma enhanced ALD (PEALD) of highly crystalline and stoichimetric $WS_2$ using a novel W-precursor namely, tungsten hexacarbonyl [$W(CO)_6$], and $H_2S$ plasma [53]. While the hexacarbonyl based precursors have yielded the films at relatively lower temperature with the benign byproducts, unlike to the $H_2S$ molecules its plasma helps to achieve the highly crystalline as-grown $WS_2$ films [53,54]. The higher amount of energy associated with the plasma (radical $-SH^*$ for this case) helps obtaining better quality as-grown $WS_2$ films [53].

In this study, PEALD-grown crystalline-$WS_2$ was prepared as an anode in NIBs for the first time. The as-grown material was well-characterized and then applied in NIBs without any post-deposition treatment. Growth of three-dimensional nano-flakes with increasing ALD cycles was found to be an additional advantage of the current recipe for obtaining high-surface area electrode for energy storage. An optimized numbers of ALD cycles were found out to achieve the maximum areal capacity from the battery. These thin films of anodes were also tested with different current density to establish the stability of this pure-$WS_2$ without any binder. Our findings provide a fundamental guideline for designing nano-structured $WS_2$ as well as transition metal sulfide (TMS)-based materials for NIBs.

## 2. Experimental

### 2.1. Material synthesis

Thin films of tungsten disulfide ($WS_2$) were prepared using a shower-head type PEALD reactor (Lucida M100-PL, NCD Technology, Republic of Korea). Tungsten hexacarbonyl [$W(CO)_6$] was used as precursor while $H_2S$ plasma served the purpose of the reactant. The $H_2S$ gas flow and the RF plasma power during all the reactions were fixed at 50 standard cubic centimeters per minute (SCCM) and 100 Watt, respectively. An optimized pulsing time of 10s for both the precursor as well as the reactant was set which helped to grow the $WS_2$ films that ensure the self-limiting growth of these films. High purity Ar gas of 200 SCCM was used as a purging gas. The purging time of 10s in-between the consecutive precursor and reactant dose assured the successful removal of the reaction by-products and the excess chemical out of the reaction chamber. To achieve a better vapor pressure and smooth transfer of the precursor, it was heated at 40 °C during the reaction and an overhead 50 SCCM Ar gas was used as carrier gas. In addition, the precursor and reactant delivery lines were also kept at 100 °C to avoid any unwanted condensation of them during the reaction. The ALD $WS_2$ films were grown at 350 °C to achieve a crystalline phase of the as-deposited material [53]. For material characterizations, the films were grown on $SiO_2/Si$ substrate and for electrochemical tests the material was directly deposited on stainless steel (SS) coin having a diameter of 1.5 cm (corresponding to an area of ~1.77 $cm^2$). To carry out the thickness dependent electrochemical performance, $WS_2$ films were grown with five different thicknesses corresponding to 200, 300, 400, 500 and 600 ALD cycles. For convenience, these samples are termed as WS200, WS300, WS400, WS500, and WS600 in rest of the article.

### 2.2. Material characterizations

PEALD grown $WS_2$ films were thoroughly studied by several spectroscopic analyses instruments. Grazing incidence X-ray diffraction (GI-XRD) (PANalytical X′-pert MRD with Cu-Kα radiation at 1.5 kW) analysis was performed to determine the crystalline nature of the as-grown films and the corresponding crystalline planes. The scanning electron microscopy (SEM, Hitachi, S-4800) were carried out to study the film's morphology changes with increasing ALD cycles. Plan-view transmission electron microscopy (TEM, Tecnai F20 equipped with a 200 kV accelerating voltage and a field emission gun) and cross-sectional view TEM analyses on SS substrates after sample preparation using focused ion-beam (FIB, Helios Nanolab G3 UC) were also performed to further confirm the crystalline phase as well as the microstructure (and layered structure) of the material. Energy dispersive spectroscopy (EDS) analysis at scanning TEM (STEM) mode was used to confirm the uniform presence of the elements (W and S) on the SS substrates. Raman spectroscopy (HORIBA XploRA Plus with a 532-nm incident laser) was used to determine the in-plane and out of plane Raman active mode in $WS_2$. In addition, the X-ray photoelectron spectroscopy (XPS, Thermo Fisher Scientific Inc., K-Alpha + XPS Spectrometer in Korea Basic Science Institute at Busan, Republic of Korea) was also performed of the as-grown films to confirm the elemental presence and to find the oxidation states of W and S in the films.

### 2.3. Electrochemical cell fabrication and measurements

Coin cells (2032-type) were fabricated using PEALD-grown $WS_2$ anode in a half-cell configuration against Na metal inside a glove box. The $WS_2$ films directly grown on SS coin was used as an active material and tested against Na metal as an anode without any further modification. Therefore, the electrode fabrication in this case differs a lot from the conventional electrode fabrication where carbon and suitable binder are mixed with the active material and the mixture slurry is tape-casted on a current collector like Cu, Al or SS foil. While Na metal and glass fiber were used as a counter electrode and separator, respectively, 1 M $NaPF_6$ dissolved in 1:1 (by volume) ethylene carbonate and dimethyl carbonate (EC/DMC) solvent was used as an electrolyte. Cyclic voltammetry (CV) measurements of the cell was performed in a potentiostat (IVIUMn-STAT, Netherlands) within a potential window of 0.01–3 V with a scan rate of 0.2 mV/s. Charge-discharge cycling measurements for all cells with different thickness were carried out within a potential window of 0.01–3 V in a battery testing unit (SE-18603, Famtech). The electrochemical impedance spectroscopy (EIS) analysis was also performed in the same potentiostat used for CVs within the frequency ranging from 100 kHz to 0.01 Hz. All of the electrochemical measurements were carried out at room temperature condition.

## 3. Results and discussion

Prior to study the morphology of the films deposited with increasing ALD cycles, the material was characterized in detail with several spectroscopic analyses. Fig. S1 shows such several *ex-situ* characterizations of the as-grown $WS_2$ films to precisely confirm the material. The GI-XRD (incident angle 3°) pattern shows the highly poly-crystalline nature of the films grown on $SiO_2$/Si substrate (Fig. S1a) using 200 ALD cycles. Three distinct peaks in the XRD pattern at 14.3, 28.7 and 33.6° can be ascribed to the (002), (004), and (101) planes, respectively, of hexagonal-$WS_2$ (JCPDS # 00-008-0237, Space group P63/mmc). However, a preferential growth in the Z-axis (perpendicular to the plane of the film in XY direction) is evident from an intense XRD peak in (002) direction along with the presence of its parallel (004) planes. This is in complete agreement with the growth of any other layered TMDCs like $MoS_2$. Such, highly poly-crystalline growth of ALD $WS_2$ at relatively low temperature of 350 °C could be attributed to the $H_2S$ plasma that provides more energetic and reactive $-SH^*$ radicals during the reaction [53]. This observation could be cross-examined by the facts that the all the binary compounds prepared by thermal ALD using hexacarbonyl based precursor generally form amorphous or amorphous-like structure in nature and when plasma is introduced as an reactant the crystalline films were obtained [31,53–55]. The Raman spectroscopy of these as-grown $WS_2$ films on $SiO_2$/Si was further confirmed as shown in Fig. S1b. The most two prominent first order Raman vibrations present in $WS_2$, namely $E^1_{2g}$ and $A_{1g}$, were approximately centered at 360 and 423 $cm^{-1}$, respectively. These in-plane ($E^1_{2g}$) and out-of-plane ($A_{1g}$) vibrations in S–W–S structure is also shown by the schematic in the inset of the Fig. S1b. In addition, the peak assigned to $E^1_{2g}$ in-plane vibration also includes the second order phonon vibration mode which is known as 2LA(M) and located at ~351 $cm^{-1}$. The relatively broad peak with larger base width (~340-371 $cm^{-1}$) is caused by the superposition of these two signature peaks located very close to one another. On the other hand, the intensity of the out-of-plane $A_{1g}$ mode is higher as it adds up for several layers of $WS_2$ in the film. All of these observations in the Raman spectra of this PEALD grown $WS_2$ are in line with the bulk $WS_2$ as well as with the thin films of it as reported earlier [38,43]. The individual scans of W and S as obtained from the XPS of the PEALD-grown $WS_2$ film is further shown in Figs. S1c and d. The complete XPS survey of the material that depicts the different electronic states of W and S is also shown in Fig. S2. The presence of considerable O1s and C1s either came from the surface oxide (or contamination) or indicated certain amount of residual carbonyl (CO) ligands present in the bulk film during the deposition. The binding energies of W4$f_{7/2}$ and 4$f_{5/2}$ electrons are located at *ca.* 32.7 and 34.9 eV respectively confirms the $W^{4+}$ oxidation states in the film. In addition, the presence of W4$p_{3/2}$ centered at ~38.4 eV along with this W4*f* peaks is also in good agreement with the existing literatures showcasing the XPS of $WS_2$. On the other hand, the peaks corresponding to S2$p_{3/2}$ and 2$p_{1/2}$ orbital electrons centered at binding energy of 162.4 and 163.9 eV, respectively, also confirms the presence of $S^{2-}$ in the films.

Plan-view and cross-sectional view SEM images of the $WS_2$ films were grown with five different ALD cycles (200, 300, 400, 500 and 600 cycles) at 350 °C and is shown in Fig. 1a and b, respectively. A two-dimensional (2D) uniform growth of $WS_2$ film (~21 nm) was observed for the WS200 sample. In addition, very few three-dimensional (3D) nano-flakes could also be seen from the plan-view SEM image of this WS200 film. On the other hand, prominent 3D nano-flake formations were evident for rest of the samples grown by increasing number of ALD cycles. For the samples WS300 and WS400, the nano-flakes were increased in both lateral and vertical dimension as shown by the SEM images. Thereafter, for WS500 and WS600 samples, the heights of the nano-flakes are not found to increase any more. On the other hand, the growth in the lateral dimension of these flakes was observed for these samples. The nano-flakes became very thick with 600 ALD cycles compared to all the other samples deposited with less number of ALD cycles. The SEM analyses thus revealed that the PEALD of $WS_2$ in this current work consists of two different stages of growths. Fig. 1c depicts the schematic of a two-stage ALD growth of this material where in the second stage of film's growth, the formation of vertical self-standing 3D nano-flakes takes place on a 2D thin film of the same. Such 3D growth, however, does not violate the typical ALD growth mechanism and it can still follow the self-limiting mechanism. Rather, similar growth was observed during ALD of $MoS_2$ or $MoSe_2$, and $V_2O_5$ where such 3D flakes formation was clear

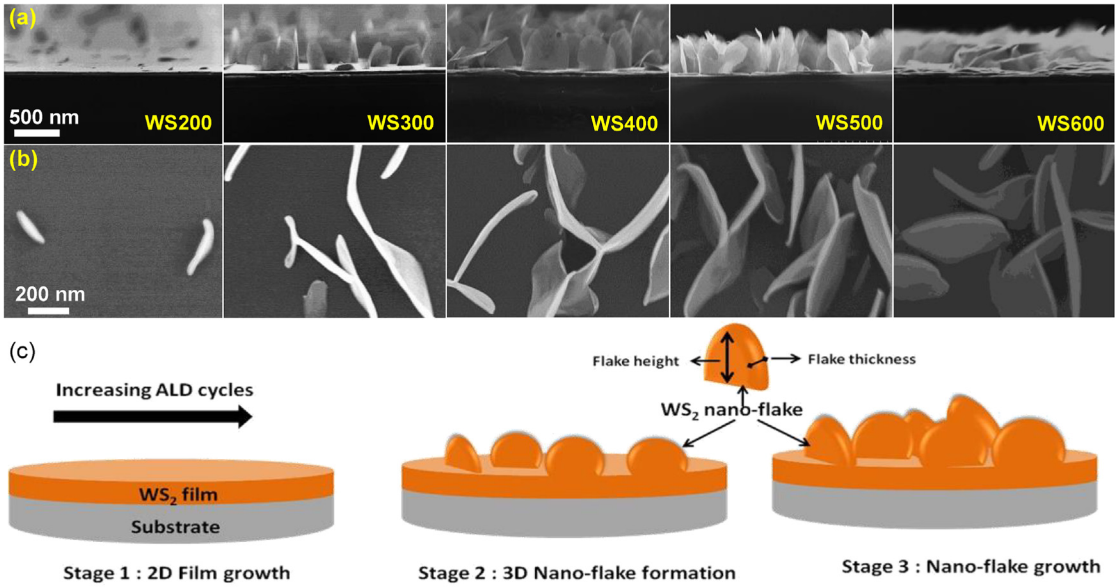

**Fig. 1.** (a) Plan and (b) cross-sectional view SEM images of the $WS_2$ films grown by 200, 300, 400, 500 and 600 ALD cycles as mentioned on the respective images, (c) the schematic depicts a two-stage film growth during PEALD of $WS_2$.

[46,56–58]. The transition from quasi 2D film to 3D island growth during ALD of $HfO_2$ was investigated and further modeled in details [56]. Randomly oriented flakes were observed for ALD-$MoSe_2$ grown preferentially in (002) direction at a relatively higher temperature using $MoCl_5$ precursor and $[(CH_3)_3Si]_2Se$ as a Se-source [57]. It should be also noted here that the flake-type 3D growth was not observed using $Mo(CO)_6$ precursor at lower deposition temperature which resulted in amorphous (or poorly crystalline) films. Furthermore, E. Østreng et al. observed a similar kind of two-stage growth during ALD of $V_2O_5$ where a 2D film was followed by formation of 3D flakes formation with increasing ALD cycles [58]. They have identified the appearance of another predominant crystallographic planes in [010] direction in addition to [001] which accelerated such 3D growth on an initial 2D flat surface. Further, in the regime of 2D film's growth up to certain number of ALD cycles the intensity of [001] direction continuously increased indicating a faster growth in the substrate's plane. Therefore, the predominant growth of the planes belong to {*00l*} family. They have further explored the as-grown 3D $V_2O_5$ as promising anode in Li-ion batteries. Similarly, in the case of TMDCs, the reason might be due to the highly preferential growth of them in [002] direction followed by the appearance of different peaks not perpendicular to c-axis which results in the formation of vertical flakes as the growth continues with increasing thickness. In our previous report, we have clearly observed the increase in the intensity of (002) peak as the number of initial ALD cycles increased from 30 to 100 [53]. Additionally, no other XRD peak was observed for those films. However, in the current study, when the XRD was performed for $WS_2$ films grown with 200 cycles, the additional appearance of the peak from (004) planes [parallel planes to (002)] indicates the further increase in the preferential growth along with the presence of (101), which is the prism plane of hexagonal close packed structure, indicating the beginning of the flakes' formation in the vertical direction. To further confirm this, we have carried out the GI-XRD of $WS_2$ film grown with 400 and 600 cycles on SS substrates. The WS600 reveals the dominant XRD peaks corresponding to (101) and (103) while the peak for (002) is suppressed and becomes invisible. Nevertheless, such growth of 3D nano-flakes for any TMDCs via different synthesis routes is a common phenomenon and often not discussed or assigned to different factors including crystallnity of the material under consideration. The 3D $WS_2$ flakes formation could be also influenced by some CVD-like growth at a higher temperature where a reaction dominated by the decomposition of the precursor $[W(CO)_6]$ might occur. However, further studies are necessary to understand the exact cause of such two-stage growth which is kept for the future scope of this current work.

Fig. S3a shows plan-view bright-field TEM image of PEALD-$WS_2$ grown with 20 cycles where nano-crystalline grains of $WS_2$ with the grain size ranging from ~3 to 10 nm is revealed. However, both the single crystal mono-layers in a shape of a triangle as well as few layered structures are further evident from the high-resolution TEM (HRTEM) image as indicated by the yellow squares and circles in Fig. S3b. The interplanar spacing (*d*-value) calculated from the lattice array (Fig. S3c) could be assigned to different planes of crystalline $WS_2$. Furthermore, the selected area electron diffraction (SAED) pattern of these films (Fig. S3d) shows the concentric rings confirming the polycrystalline nature of the films. In addition, we have performed the analysis of the $WS_2$ grown on SS substrate which was used as an electrode in NIBs without any further treatment. The cross-sectional TEM (XTEM) analysis (Fig. 2a-b), HRTEM image (Fig. 2c), STEM-HAADF (scanning TEM-high angle annular dark field) image (Fig. 2d), and STEM-EDS elemental mapping (Fig. 2e-i) of the WS400 on SS substrate also ensured the 2-stage growth of crystalline-$WS_2$ on SS substrate. While the distinct interface between SS substrate and the nano-flakes could be realized from Fig. 2a, the 2D base and 3D flakes are also evident from magnified XTEM image (Fig. 2b). Moreover, the thickness of 2D base film and the flake height are estimated as ~23.5 and 116.7 nm, respectively. The 2D base thickness (20–25 nm) beyond which the nano-flake started growing therefore remains similar both on $SiO_2$/Si or SS substrate as seen from SEM and TEM analyses. It reassures us the nearly similar growth of this PEALD-$WS_2$ on $SiO_2$/Si or SS substrates. Similar observations were also made by E. Østreng et al. during the two stage growth of ALD-$V_2O_5$ [58]. Therefore, the PEALD process parameters should have a more determining role in such two-stage growth of $WS_2$. However, the growth behavior might not be absolutely independent of the

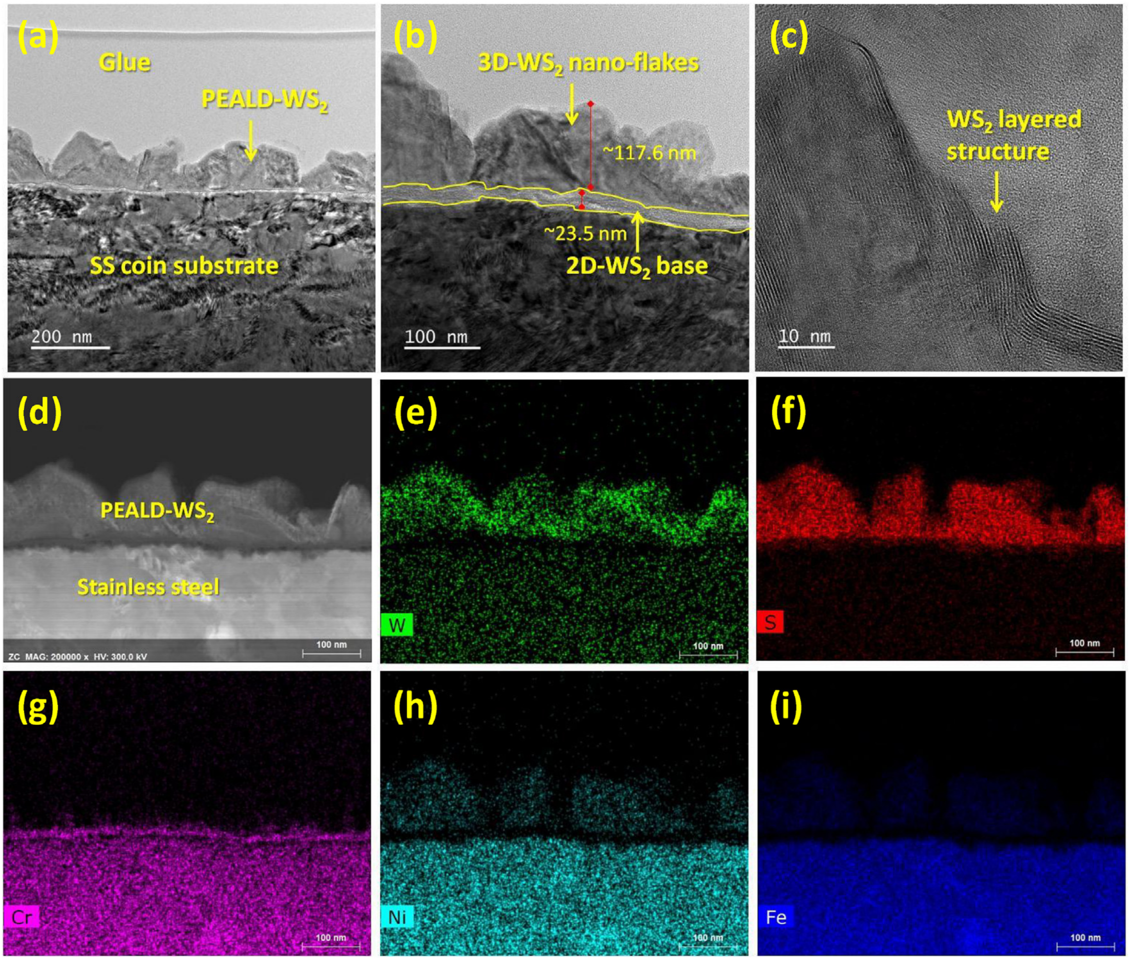

**Fig. 2.** (a–b) XTEM and (c) HRTEM images of the WS400 grown on SS substrate, (d) HAADF image of the same, and (e–i) STEM-EDS mapping results confirming the individual elements present in the film and the substrate.

substrates especially with respect to the thickness of the $WS_2$ layer beyond which the nano-flakes growth would prevail. In addition, HRTEM image (Fig. 2c) reveals the layered structure of the $WS_2$ films on SS substrate as well. Edge defects are also identified in HRTEM image which might be in favor of sodiation process by providing more chemically active sites at these edge defects. The STEM-HAADF image (Fig. 2d) and its corresponding STEM-EDS elemental mapping (Fig. 2e-i) shows the individual elements (FW and S) present uniformly in the film along with the elements (Cr, Ni and Fe) in the substrate by confirming the $WS_2$ nano-flakes deposited on SS substrate without any further doubt. One might notice the diffusion of W into the SS as well as similar effect for Ni and Fe inside the $WS_2$ layer in the STEM mapping. However, we would like to interpret such phenomenon owing to artifacts from the background such as substrate, grid, pole piece, holder etc. which are associated with the sample preparation using FIB technique and TEM analysis. Similar effects are also observed during the post-cycling STEM analyses of the sample as shown later in the article. The SS substrate is not only stable for fabricating electrodes but also is well expected not to react chemically during or after the $WS_2$ growth. A sharp interface between the SS and film observed in the XTEM images further supports our claim. The electron diffraction pattern of this film at two different spots further reveals the presence of W and S on SS substrate as shown in Fig. S4. Thus, all of the *ex-situ* characterizations reveal the formation of polycrystalline films with highly preferential growth in (002), stoichiometric $WS_2$ deposited by PEALD.

Fig. 3a shows the CV measurements of the PEALD-$WS_2$ grown by 200 ALD cycles within a potential window of 0.01–3 V with a scan rate of 0.2 mV/s. The first cathodic sweep (discharge cycle) shows three prominent peaks at 1.2, 0.87 and 0.6 V *vs.* $Na/Na^+$. While the first two peaks at higher potentials (1.2 and 0.87 V) could be assigned to the multi-step insertion of Na-ions into the $WS_2$ matrix ($4Na^+ + WS_2 + 4e^- \rightarrow Na_4WS_2$) and the conversion reaction between them has taken place corresponding to 0.6 V ($Na_4WS_2 \rightarrow 2Na_2S + W$). In addition, a relatively smaller intense peak could be observed at around 0.35 V which is attributed to the solid electrolyte interphase (SEI) formation during the discharge cycle. The multistep intercalation or the SEI formation in $WS_2$ anodes in NIBs during cathodic cycle are in well agreement with existing literatures [41]. However, SEI deformation was also evident in this case as revealed by a broad shoulder peak at ~0.39 V during the anodic sweep (charge cycle) of the CVs. Such reversible formation-deformation of organic SEI is beneficial which adds into the capacity and probably slows down the capacity feeding at the same time [39]. The removal of the Na-ion from the electrode ($Na_2S + W \rightarrow Na_xWS_2 \rightarrow Na + WS_2$) are reflected by the three consecutive peaks during the charge cycles at 1.4, 1.9 and 2.3 V corresponding to the reversible conversion reaction and multiple deintercalation, respectively. While the anodic peaks are not shifted upon cycling, a considerable shift in the cathodic peaks is observed in the second cycle. All the peaks corresponding to multiple Na-intercalations as

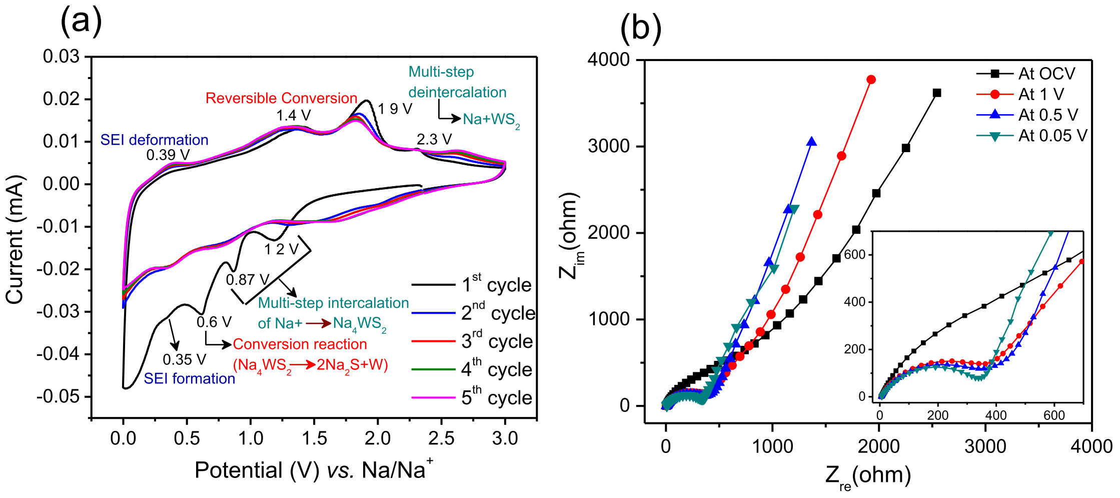

**Fig. 3.** (a) CVs of the PEALD grown WS200 anode within a potential range of 0.01–3 V at a scan rate of 0.2 mV/s and (b) Nyquist plot for the same anode at four different potentials during cathodic sweep.

well as the conversion of $WS_2$ to $Na_2S$ are taken place at higher potential which is caused by the change in the chemical environment after first cycle. However, all the peaks remain unaltered from second cycle onwards revealing the high reversibility of the reactions between Na and $WS_2$. From second cycle onwards, the two-step intercalations occurred corresponding to peaks at 1.6 and 1.3 V followed by the conversion reaction assigned by the peak at ~0.77 V. The cathodic peaks at higher potential also indicate easier sodiation after the first cycle which enlarges the interatomic space enhancing the Na-insertion. Similarly, the reversible SEI formation was observed at 0.35 V from second cycle onward. On the other hand, all the oxidation peaks in the charging cycles are perfectly repeatable from the first cycle itself except for the oxidation peak at 2.3 V which shifted to 2.6 V from second cycle onward. The additional peak for SEI layer breaking during charging cycle also remains at the same potential from the beginning. None of the earlier CVs related to $WS_2$ anode in NIBs reflected all of these peak together. As a consequence, one can observe different explanations to the possible electrochemical reactions and their corresponding potentials during both cathodic and anodic sweeps for $WS_2$ anodes used in NIBs [39–42,44]. Therefore, we could claim that the thin films of $WS_2$ anodes without any binder and carbon might be an ideal approach to confirm and study all the possible reactions during charge-discharge cycles. Fig. 3b shows the Nyquist plots for WS200 anode as obtained from the EIS measurements at different potentials during discharging. Four different potentials were chosen according to the electrochemical reactions observed in CV, which were at open circuit voltage (3 V), after the Na-intercalation took place (1 V), at 0.5 V above which the conversion reaction took place, and at almost complete discharge state (0.05 V).

The inset of Fig. 3b shows a zoom view of the impedance spectra at high-frequency range. The charge transfer resistance ($R_{ct}$) is significantly reduced when the Na intercalated into the film. The $R_{ct}$ values estimated from the diameter of the semi-circle with real impedance ($Z_{real}$) co-ordinate at OCV and at 1 V are approximately 1367 and 468.8 Ω, respectively. While the lowest charge-transfer resistance of ~387.4 Ω was calculated at almost complete discharge state (0.05 V), the relative increase in the solution/electrolyte resistance ($R_s/R_e$) from 4.3 to 6.4 Ω complements the drop of $R_{ct}$. Table S1 represents the $R_{ct}$ and $R_s$ values at different potentials. Thus, the EIS analyses reflect the significant resistive nature of pristine $WS_2$ in absence of any conducting C in the electrode. Therefore, an optimization of the electrode thickness (or dimensions in general) is quite necessary to replace the carbon based anodes with a conversion-based anode like $WS_2$. The incorporation of Na (or presence of W in case of complete conversion of $WS_2$) decreases the resistivity (or overall resistance) of the electrode and hence the $R_{ct}$.

Once the CVs confirmed the stable and reversible redox reactions of the $WS_2$ thin-film anode against Na-ion, we further perform the charge-discharge cycles of the films grown with increasing number of ALD cycles. Fig. 4a shows the first charge-discharge profiles of these five different anodes grown by 200, 300, 400, 500, and 600 ALD cycles. The areal discharge capacity was increased from ~66 to ~88 μAh/cm$^2$ corresponding to the anodes grown by 200 and 400 ALD cycles, respectively. Such significant increase over 33% in the discharge capacity is contributed by the additional amount of the anode material, more especially, owing to the 3D nano-flake growth with increasing ALD cycles that provides much higher interface between $WS_2$ and electrolyte that directly enhanced the amount of Na-insertion into the material. However, as shown in the SEM images of these films, there was only lateral growth of these flakes and their increasing density beyond 400 ALD cycles that only made these 3D flakes more thick and leaving less space among them. This phenomenon caused the capacity of the cell to decrease when the ALD cycles were increased further to 500 and 600 cycles. In the case of WS600, the discharge capacity at the first cycles was found even lower (*ca.* 53.5 μAh/cm$^2$) than the WS200 anode. Therefore, it can be concluded that the 3D feature of any thin films is beneficial up to a maximum dimension (both lateral and vertical) beyond which it should lead to deteriorate the performance of the cell due to the high resistance and excessive longer path for the movement of electrons and the ions. In addition to obtain the condition for achieving maximum discharge capacity, the charge-discharge profiles give the complementary information to that of CVs about the Na-insertion and deinsertion process. While the prominent plateau between 1.8 and 1.2 V in the discharge profile reflects the Na-insertion into the $WS_2$ matrix, another relatively broad plateau between 0.8 and 0.5 V stands for the conversion based reaction. On the other hand, the broad multiple plateaus within 1.0–2.0 V in the charge profiles indicates the multiple Na-deinsertion process from the $Na_xWS_2$ matrix. Similar optimizations with increasing ALD cycles were further observed from the cycling measurements of these anodes.

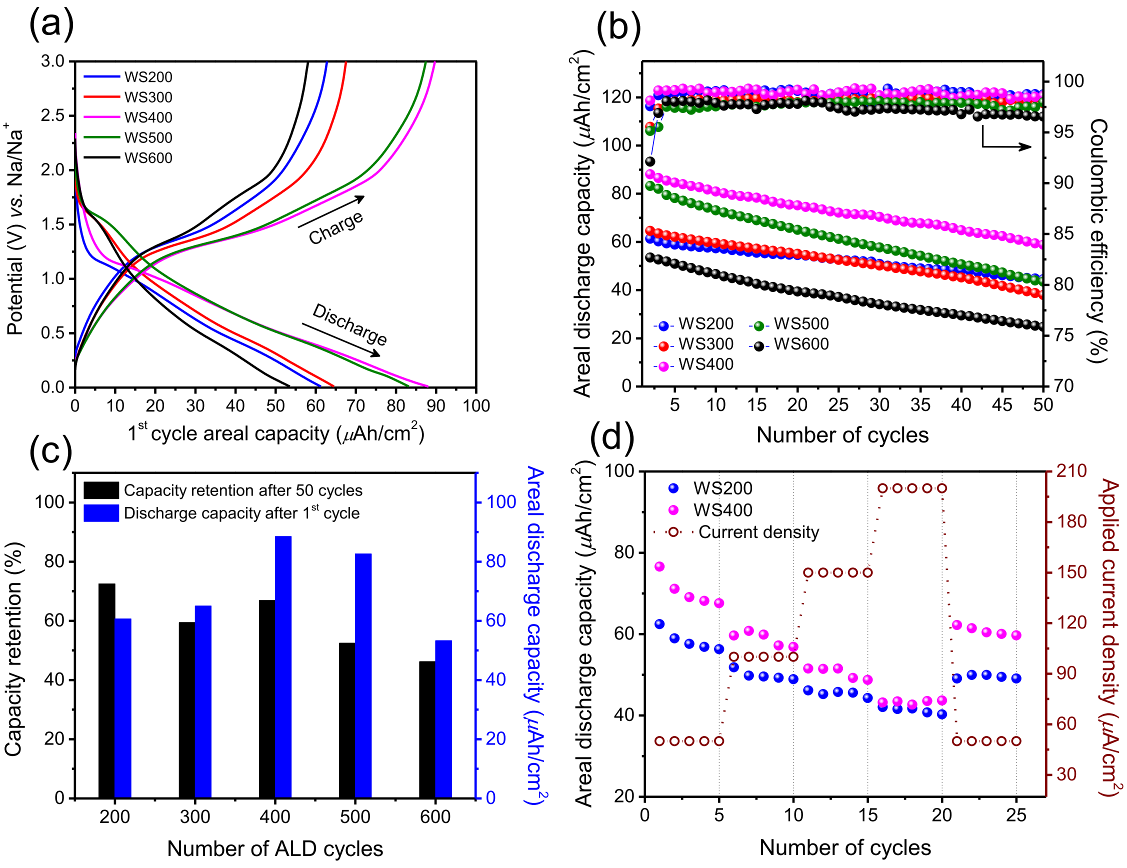

**Fig. 4.** (a) First charge-discharge profiles, (b) the discharge capacities and corresponding Coulombic efficiencies for 50 charge-discharge cycles at a current density of 50 μA/cm², and (c) the capacity retention and the discharge capacity after at 50th discharge cycle of five different $WS_2$ anodes, and (d) the rate-performance with different current densities for WS200 and WS400 anodes.

Fig. 4b shows the discharge capacities of these anodes and their corresponding Coulombic efficiencies (CEs) up to 50 charge-discharge cycles at a current density of 50 μA/cm$^2$. Similar significant increase in the capacity was observed for WS400 anode compared to the WS200 one. On the other hand, the discharge capacities again decreased for the anodes WS500 and WS600. The areal discharge capacities of approximately 44.5, 58.8 and 24.7 μAh/cm$^2$ were estimated at the 50th cycle for WS200, WS400 and WS600 cycles anodes, respectively. Though the areal capacity may seem low, the specific capacity would be extremely high for the ALD grown pristine electrodes owing to the significantly low mass loading of the active electrode in μg range. The two-stage growth of the $WS_2$ film gives rise to an almost flat surface up to 200 cycles with an average thickness of 20–25 nm of the film. Considering the theoretical bulk density of $WS_2$ as 7.5 g/cm$^3$, the areal mass loading of the electrode grown with 200 ALD cycles (25 nm thickness) can be estimated as ~18.75 μg/cm$^2$. Now, the mass loading could be considered as a linear function of number of ALD cycles and hence the approximate mass loading would be 37.5 μg/cm$^2$ for the electrode grown with 400 ALD cycles. Such low mass loading indeed would reflect very high specific capacity. Though the estimated specific capacities (in mAh/g) for WS400, WS500 and WS600 at their respective current rate (calculated in mA/g) values are tabulated in S2, a very high current rate has to be accommodated to apprehend a realistic specific capacity for these thin film's based electrodes. While the mass loading in case of ALD-$V_2O_5$ electrode mentioned earlier could be found similar to the current study, the authors reported a current rate up to as high as 141 A/g [58]. Moreover, the specific capacities for different electrodes reported in the Table S2 might not be compared directly because of the difference in the applied current density per unit mass. However, still one can easily recognize the deterioration of the NIB anodes prepared with higher number of ALD cycles beyond 400. Therefore, we refrain and do not recommend to estimate the specific capacity for films with lower mass loading than 0.1 mg/cm$^2$which could lead to a severe error for a minimum error in the mass calculation. Such recommendation are also made earlier for thin film electrodes grown by ALD or by any other similar technique [59,60]. The primary reason behind this higher specific capacity obtained for this case might be due to the significantly lower mass loading compared to the electrodes fabricated with the conventional process. Secondly, an extremely thin uniform film with further uniformly distributed 3D architecture could also facilitate an easier Na-intercalation than the previously reported similar electrodes. Nevertheless, we would prefer to conceive the idea of optimization through areal capacity against a constant areal current density for such case.

The CEs for WS200, WS300 and WS400 anodes were found to be more than 99% over 50 charge-discharge cycles as also shown in Fig. 4b. However, the CEs also seem to decrease, though relatively less in magnitude, for 500 and 600 cycles anodes. The CE is found around 96–97% for the WS600 electrode which showed lowest capacity in the cycling test. Thus, the CEs are also in good agreement with the earlier observations on ALD cycles dependant performance of the $WS_2$ anodes. However, another interesting thing to notice here is that though the discharge capacity initially increases with formation of 3D $WS_2$ nano-flakes, the capacity retention for all of the anodes is lower than the WS200 anode. The highest capacity retention of around 72.5% after 50 cycles (Fig. 4c) was found for WS200 anode which can be considered as a satisfactory value for this pristine $WS_2$ films in absence of conducting carbon. In this regard, considerably high capacity retention of 66.8% was also achieved for WS400 which resulted in much higher areal capacity of this film compared to WS200 anode even after 50 charge-discharge cycles. On the other hand, the poor initial capacity along with lowest capacity retention (~46%) makes WS600 anode worst among all. Therefore, from the charge-discharge cycling and capacity retention profile, we recommend 400 ALD cycles as an optimum condition for growing the $WS_2$ anodes for this particular case. However, such optimal condition might differ depending on the material's property, growth rate, and morphology, if present, for some other ALD grown materials.

Fig. 4d shows the discharge capacities at four different current densities ranging from 50 to 200 $\mu A/cm^2$. We have chosen both the anodes of WS200 and WS400 as the former has highest capacity retention and the later has highest discharge capacity. Though the discharge capacities at low current densities (50 and 100 $\mu A/cm^2$) are significantly higher for the 400 cycles anode but, the capacity does not differ much at 150 $\mu A/cm^2$ current density. Interestingly, the discharge capacities become almost same (~42 $\mu Ah/cm^2$) for both these electrodes when the charge-discharge was performed at further high current density (200 $\mu A/cm^2$). Nevertheless, the discharge capacities were again restored (~50 and 60.5 $\mu Ah/cm^2$ for WS200 and WS400 anodes, respectively) with similarly significant difference when the current density was decreased to 50 $\mu A/cm^2$. The reason for such observations could be correlated with the insufficient time for charge-discharge process at higher current densities which did not allow the complete sodiation-desodiation process for WS400 anode which has higher overall electrical resistance than the WS200 anode. As a result, at very high current density, similar equivalent amount of $WS_2$ is capable to undergo the fast charge-discharge process in both the cases, yielding same areal capacity for WS200 and WS400 anodes. Therefore, it can now be inferred that the performance of any high-surface 3D films in such application not only depends on the dimensional aspects of the films but also strongly on the operational parameters like current density. Similar effects on power cycles' performance influenced by the overall resistivity of the different $WS_2$ (bare and mixed with rGO) anodes are also observed in case of Li-ion batteries [37]. In spite of the capacity fall at higher current densities, the 3D growth of $WS_2$ via PEALD in this particular case gives a room for a direct synthesis of the material with superior performance in NIBs at low as well as moderate current densities. However, the capacity fading as well as the rate capability for TMDCs used in NIBs could be further enhanced with novel designing, e.g. by introducing defects to the 2D layered structure or by adding extra S to the architecture as demonstrated in case of $MoS_2$ anodes [61,62].

The post-cycling XTEM analyses of the optimum electrode (WS400) are performed further at full-discharge state (0.01 V). Fig. 5a shows the XTEM images revealing significantly distorted 3D nano-flakes structure after several sodiation-desodiation processes but the 2D base structure was almost intact (Fig. 5b). This indicates that such ALD growth indeed a favorable aspect for any energy storage applications where the material is in very well adhere to the substrate while simultaneously it provides a higher surface area through the 3D nano-flakes formation. The HRTEM image (Fig. 5c) further confirms predominant amorphous film after the complete sodiation that indicates the formation of amorphous $NaWS_2$ and/or $Na_2S$ phases. However, several small nano-crystalline grains also could be identified in the HRTEM image. The very poor crystalline nature of the sodiated film is further supported with the diffused rings observed in the SAED pattern (inset of Fig. 5c), which is clearly different from those of the as-grown PEALD-$WS_2$ film (Fig. S3d). The estimated d-value of 0.26 nm corresponding to this diffused ring hints at the presence of certain amount of crystalline $WS_2$ in the film. Therefore, this post-cycling TEM analysis also helped us to realize the declining performance of the anodes grown with higher number of ALD cycles (beyond 400). On the other hand, the STEM-

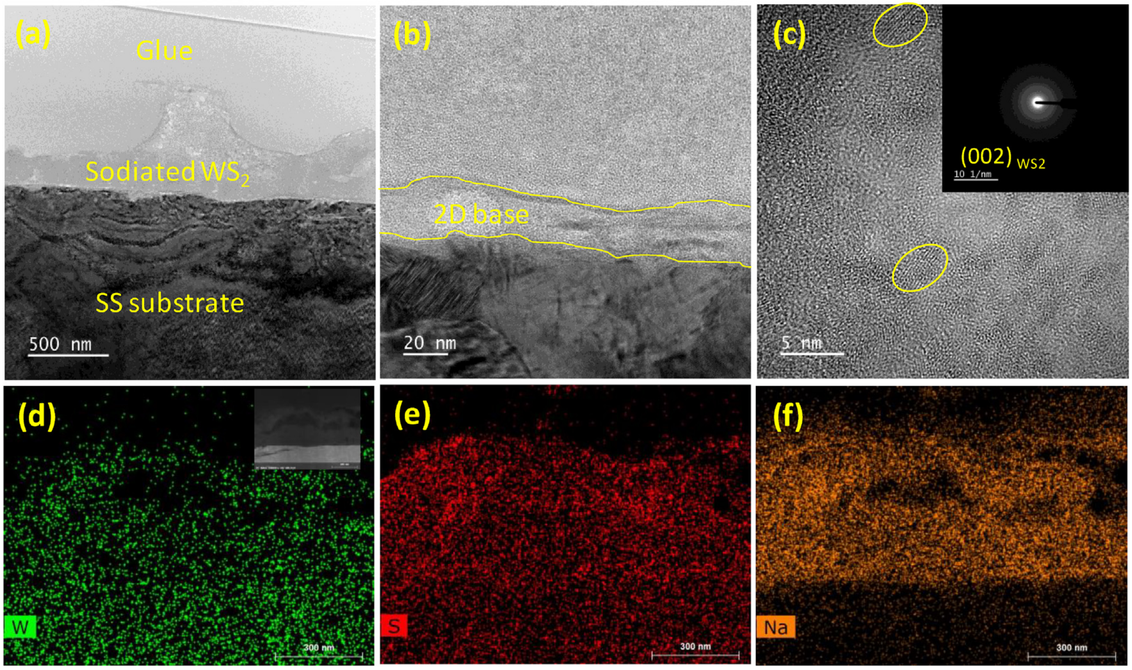

**Fig. 5.** (a–b) Cross-sectional view TEM images of the WS400 samples in full-sodiated state (c) HRTEM image and SAED pattern (inset) revealing that some nano-crystalline $WS_2$ might be present after complete discharge, and (d–f) the STEM-EDS mapping of W, S, Na in the film.

EDS elemental mapping of the film confirms the uniform presence of Na in the complete film establishing a smooth intercalation on the Na-ions into these ALD-grown WS$_2$ films. Further the ED-spectra (Fig. S6) taken at different spots of the film also confirmed the presence of Na along with W and S on SS substrate.

## 4. Conclusions

Stoichiometric, polycrystalline WS$_2$ films in preferential (002) direction were grown by PEALD. The usage of H$_2$S plasma caused such crystalline growth of WS$_2$ films at a relatively low temperature of 350 °C by providing highly energetic and reactive $-SH^*$ radicals. Formation of 3D nano-flakes with increasing ALD cycles provides more surface area which potentially affects any kind of further applications of these films. Therefore, these PEALD-WS$_2$ films are directly grown on SS substrates with different ALD cycles and then used as an anode in NIBs. The CVs of the WS$_2$ films showed stable reversible intercalation and conversion reactions against Na-ion with prominent redox-peaks revealing the high activity of such thin films. Maximum areal capacity with reasonably high capacity retention is achieved for the anode grown by 400 ALD cycles. The capacity deteriorates for further increasing the ALD cycles that leads to formation of thicker flakes restricting the movements of Na-ions inside. The rate capability study also reflects the stability of these thin film electrodes over a wide range of current densities. The study overall conveys the importance of PEALD toward synthesizing crystalline TMDC, like WS$_2$ with an optimum number of ALD cycles and to use these films directly as an anode in NIBs. However, the approach can be extended for any other ALD-grown material and by depositing them optimally on some 3D conducting template, the capacity can further be enhanced.

## Acknowledgements

This work was financially supported by 2017 Yeungnam Univeristy Research Grant. The precursor used in this study was provided by UP Chemical Co. Ltd., Korea.

## Appendix A. Supplementary data

Supplementary data to this article can be found online at https://doi.org/10.1016/j.electacta.2019.134766.

## References

[1] A. Sumboja, J. Liu, W.G. Zheng, Y. Zong, H. Zhang, Z. Liu, Electrochemical energy storage devices for wearable technology: a rationale for materials selection and cell design, Chem. Soc. Rev. 47 (2018) 5919–5945.

[2] J.Y. Yong, V.K. Ramachandaramurthy, K.M. Tan, N. Mithulananthan, A review on the state-of-the-art technologies of electric vehicle, its impacts and prospects, Renew. Sustain. Energy Rev. 49 (2015) 365–385.

[3] Q. Zhang, Q.-F. Dong, M.-S. Zheng, Z.-W. Tian, Electrochemical energy storage device for electric vehicles, J. Electrochem. Soc. 158 (2011) A443–A446.

[4] M.F. El-Kady, Y. Shao, R.B. Kaner, Graphene for batteries, supercapacitors and beyond, Nat. Rev. Mater. 1 (2016) 16033.

[5] W. Zuo, R. Li, C. Zhou, Y. Li, J. Xia, J. Liu, Battery-supercapacitor hybrid devices: recent progress and future prospects, Adv. Sci. 4 (2017), 1600539.

[6] N. Nitta, F. Wu, J.T. Lee, G. Yushin, Li-ion battery materials: present and future, Mater. Today 18 (2015) 252–264.

[7] H.-D. Lim, B. Lee, Y. Bae, H. Park, Y. Ko, H. Kim, J. Kim, K. Kang, Reaction chemistry in rechargeable Li–O$_2$ batteries, Chem. Soc. Rev. 46 (2017) 2873–2888.

[8] J. Lu, L. Li, J.-B. Park, Y.-K. Sun, F. Wu, K. Amine, Aprotic and aqueous Li–O$_2$ batteries, Chem. Rev. 114 (2014) 5611–5640.

[9] S. Sinha, H.V. Ramasamy, D.K. Nandi, P.N. Didwal, J.Y. Cho, C.-J. Park, Y.-S. Lee, S.-H. Kim, J. Heo, Atomic layer deposited zinc oxysulfide anodes in Li-ion batteries: an efficient solution for electrochemical instability and low conductivity, J. Mater. Chem. 6 (2018) 16515–16528.

[10] R. Kumar, J. Liu, J.-Y. Hwang, Y.-K. Sun, Recent research trends in Li–S batteries, J. Mater. Chem. 6 (2018) 11582–11605.

[11] W. Kang, N. Deng, J. Ju, Q. Li, D. Wu, X. Ma, L. Li, M. Naebe, B. Cheng, A review of recent developments in rechargeable lithium–sulfur batteries, Nanoscale 8 (2016) 16541–16588.

[12] J.-Y. Hwang, S.-T. Myung, Y.-K. Sun, Sodium-ion batteries: present and future, Chem. Soc. Rev. 46 (2017) 3529–3614.

[13] N. Yabuuchi, K. Kubota, M. Dahbi, S. Komaba, Research development on sodium-ion batteries, Chem. Rev. 114 (2014) 11636–11682.

[14] H. Kim, H. Kim, Z. Ding, M.H. Lee, K. Lim, G. Yoon, K. Kang, Recent progress in electrode materials for sodium-ion batteries, Adv. Energy Mater. 6 (2016), 1600943.

[15] K. Kubota, S. Komaba, Review—practical issues and future perspective for Na-ion batteries, J. Electrochem. Soc. 162 (2015) A2538–A2550.

[16] M.H. Han, E. Gonzalo, G. Singh, T. Rojo, A comprehensive review of sodium layered oxides: powerful cathodes for Na-ion batteries, Energy Environ. Sci. 8 (2015) 81–102.

[17] S. Guo, Q. Li, P. Liu, M. Chen, H. Zhou, Environmentally stable interface of layered oxide cathodes for sodium-ion batteries, Nat. Commun. 8 (2017) 135.

[18] K. Jiang, S. Xu, S. Guo, X. Zhang, X. Zhang, Y. Qiao, T. Fang, P. Wang, P. He, H. Zhou, A phase-transition-free cathode for sodium-ion batteries with ultralong cycle life, Nano Energy 52 (2018) 88–94.

[19] G. Fang, Z. Wu, J. Zhou, C. Zhu, X. Cao, T. Lin, Y. Chen, C. Wang, A. Pan, S. Liang, Observation of pseudocapacitive effect and fast ion diffusion in bimetallic sulfides as an advanced sodium-ion battery anode, Adv. Energy Mater. 8 (2018), 1703155.

[20] C.-H. Lim, T.-Y. Huang, P.-S. Shao, J.-H. Chien, Y.-T. Weng, H.-F. Huang, B.J. Hwang, N.-L. Wu, Experimental study on sodiation of amorphous silicon for use as sodium-ion battery anode, Electrochim. Acta 211 (2016) 265–272.

[21] M.-S. Balogun, Y. Luo, W. Qiu, P. Liu, Y. Tong, A review of carbon materials and their composites with alloy metals for sodium ion battery anodes, Carbon 98 (2016) 162–178.

[22] H. Hou, X. Qiu, W. Wei, Y. Zhang, X. Ji, Carbon anode materials for advanced sodium-ion batteries, Adv. Energy Mater. 7 (2017), 1602898.

[23] H. Kang, Y. Liu, K. Cao, Y. Zhao, L. Jiao, Y. Wang, H. Yuan, Update on anode materials for Na-ion batteries, J. Mater. Chem. 3 (2015) 17899–17913.

[24] W. Luo, F. Shen, C. Bommier, H. Zhu, X. Ji, L. Hu, Na-ion battery anodes: materials and electrochemistry, Acc. Chem. Res. 49 (2016) 231–240.

[25] R. Dong, I. Kuljanishvili, Review Article: progress in fabrication of transition metal dichalcogenides heterostructure systems, J. Vac. Sci. Technol. B 35 (2017), 030803.

[26] S. Manzeli, D. Ovchinnikov, D. Pasquier, O.V. Yazyev, A. Kis, 2D transition metal dichalcogenides, Nat. Rev. Mater. 2 (2017) 17033.

[27] T.C. Berkelbach, D.R. Reichman, Optical and excitonic properties of atomically thin transition-metal dichalcogenides, Annu. Rev. Condens. Matter Phys. 9 (2018) 379–396.

[28] W. Choi, N. Choudhary, G.H. Han, J. Park, D. Akinwande, Y.H. Lee, Recent development of two-dimensional transition metal dichalcogenides and their applications, Mater. Today 20 (2017) 116–130.

[29] J. Xiao, D. Choi, L. Cosimbescu, P. Koech, J. Liu, J.P. Lemmon, Exfoliated MoS$_2$ nanocomposite as an anode material for lithium ion batteries, Chem. Mater. 22 (2010) 4522–4524.

[30] Y. Teng, H. Zhao, Z. Zhang, Z. Li, Q. Xia, Y. Zhang, L. Zhao, X. Du, Z. Du, P. Lv, K. Świerczek, MoS$_2$ nanosheets vertically grown on graphene sheets for lithium-ion battery anodes, ACS Nano 10 (2016) 8526–8535.

[31] D.K. Nandi, U.K. Sen, D. Choudhury, S. Mitra, S.K. Sarkar, Atomic layer deposited MoS$_2$ as a carbon and binder free anode in Li-ion battery, Electrochim. Acta 146 (2014) 706–713.

[32] J. Hao, J. Zheng, F. Ling, Y. Chen, H. Jing, T. Zhou, L. Fang, M. Zhou, Strain-engineered two-dimensional MoS$_2$ as anode material for performance enhancement of Li/Na-ion batteries, Sci. Rep. 8 (2018) 2079.

[33] L. David, R. Bhandavat, G. Singh, MoS$_2$/Graphene composite paper for sodium-ion battery electrodes, ACS Nano 8 (2014) 1759–1770.

[34] R. Wang, S. Gao, K. Wang, M. Zhou, S. Cheng, K. Jiang, MoS$_2$@rGO nanoflakes as high performance anode materials in sodium ion batteries, Sci. Rep. 7 (2017) 7963.

[35] T. Stephenson, Z. Li, B. Olsen, D. Mitlin, Lithium ion battery applications of molybdenum disulfide (MoS$_2$) nanocomposites, Energy Environ. Sci. 7 (2014) 209–231.

[36] J. Huang, Z. Wei, J. Liao, W. Ni, C. Wang, J. Ma, Molybdenum and tungsten chalcogenides for lithium/sodium-ion batteries: beyond MoS$_2$, J. Energy Chem. 33 (2019) 100–124.

[37] K. Shiva, H.S.S. Ramakrishna Matte, H.B. Rajendra, A.J. Bhattacharyya, C.N.R. Rao, Employing synergistic interactions between few-layer WS$_2$ and reduced graphene oxide to improve lithium storage, cyclability and rate capability of Li-ion batteries, Nano Energy 2 (2013) 787–793.

[38] X. Fang, C. Hua, C. Wu, X. Wang, L. Shen, Q. Kong, J. Wang, Y. Hu, Z. Wang, L. Chen, Synthesis and electrochemical performance of graphene-like WS$_2$, Chem. Eur J. 19 (2013) 5694–5700.

[39] D. Su, S. Dou, G. Wang, WS$_2$@graphene nanocomposites as anode materials for Na-ion batteries with enhanced electrochemical performances, Chem. Commun. 50 (2014) 4192–4195.

[40] X. Wang, J. Huang, J. Li, L. Cao, W. Hao, Z. Xu, Q. Kang, (002)-oriented WS$_2$ with high crystalline with enhanced capacity as anode material for sodium ion batteries, J. Alloy. Comp. 696 (2017) 22–27.

[41] Y. Liu, N. Zhang, H. Kang, M. Shang, L. Jiao, J. Chen, WS$_2$ nanowires as a high-performance anode for sodium-ion batteries, Chem. Eur J. 21 (2015) 11878–11884.

[42] X. Wang, J. Huang, J. Li, L. Cao, W. Hao, Z. Xu, Improved Na storage performance with the involvement of nitrogen-doped conductive carbon into $WS_2$ nanosheets, ACS Appl. Mater. Interfaces 8 (2016) 23899–23908.

[43] Y.V. Lim, Y. Wang, D. Kong, L. Guo, J.I. Wong, L.K. Ang, H.Y. Yang, Cubic-shaped $WS_2$ nanopetals on a Prussian blue derived nitrogen-doped carbon nanoporous framework for high performance sodium-ion batteries, J. Mater. Chem. 5 (2017) 10406–10415.

[44] X. Wang, J. Huang, J. Li, L. Cao, W. Hao, Z. Xu, Q. Kang, Controlling the layered structure of $WS_2$ nanosheets to promote Na+ insertion with enhanced Na-ion storage performance, Electrochim. Acta 222 (2016) 1724–1732.

[45] X. Han, Y. Liu, Z. Jia, Y.-C. Chen, J. Wan, N. Weadock, K.J. Gaskell, T. Li, L. Hu, Atomic-layer-deposition oxide nanoglue for sodium ion batteries, Nano Lett. 14 (2014) 139–147.

[46] M.B. Sreedhara, S. Gope, B. Vishal, R. Datta, A.J. Bhattacharyya, C.N.R. Rao, Atomic layer deposition of crystalline epitaxial $MoS_2$ nanowall networks exhibiting superior performance in thin-film rechargeable Na-ion batteries, J. Mater. Chem. 6 (2018) 2302–2310.

[47] S. Sinha, P.N. Didwal, D.K. Nandi, J.Y. Cho, S.-H. Kim, C.-J. Park, J. Heo, Atomic layer deposited-ZnO@3D-Ni-foam composite for Na-ion battery anode: a novel route for easy and efficient electrode preparation, Ceram. Int. 45 (2019) 1084–1092.

[48] J. Liu, B. Wang, Q. Sun, R. Li, T.-K. Sham, X. Sun, Atomic layer deposition of hierarchical CNTs@$FePO_4$ architecture as a 3D electrode for lithium-ion and sodium-ion batteries, Adv. Mater. Interfaces 3 (2016), 1600468.

[49] T.W. Scharf, D.R. Diercks, B.P. Gorman, S.V. Prasad, M.T. Dugger, Atomic layer deposition of tungsten disulphide solid lubricant nanocomposite coatings on rolling element bearings, Tribol. Trans. 52 (2009) 284–292.

[50] B. Groven, M. Heyne, A. Nalin Mehta, H. Bender, T. Nuytten, J. Meersschaut, T. Conard, P. Verdonck, S. Van Elshocht, W. Vandervorst, S. De Gendt, M. Heyns, I. Radu, M. Caymax, A. Delabie, Plasma-enhanced atomic layer deposition of two-dimensional $WS_2$ from $WF_6$, $H_2$ plasma, and $H_2S$, Chem. Mater. 29 (2017) 2927–2938.

[51] T.W. Scharf, S.V. Prasad, M.T. Dugger, P.G. Kotula, R.S. Goeke, R.K. Grubbs, Growth, structure, and tribological behavior of atomic layer-deposited tungsten disulphide solid lubricant coatings with applications to MEMS, Acta Mater. 54 (2006) 4731–4743.

[52] M. Mattinen, T. Hatanpää, P.J. King, K. Meinander, K. Mizohata, P. Jalkanen, J. Räisänen, M. Ritala, M. Leskelä, Crystalline tungsten sulfide thin films by atomic layer deposition and mild annealing, J. Vac. Sci. Technol. A 37 (2019), 020921.

[53] S. Yeo, D.K. Nandi, R. Rahul, T.H. Kim, B. Shong, Y. Jang, J.-S. Bae, J.W. Han, S.-H. Kim, H. Kim, Low-temperature direct synthesis of high quality $WS_2$ thin films by plasma-enhanced atomic layer deposition for energy related applications, Appl. Surf. Sci. 459 (2018) 596–605.

[54] D.K. Nandi, U.K. Sen, A. Dhara, S. Mitra, S.K. Sarkar, Intercalation based tungsten disulfide ($WS_2$) Li-ion battery anode grown by atomic layer deposition, RSC Adv. 6 (2016) 38024–38032.

[55] Y. Jang, S. Yeo, H.-B.-R. Lee, H. Kim, S.-H. Kim, Wafer-scale, conformal and direct growth of $MoS_2$ thin films by atomic layer deposition, Appl. Surf. Sci. 365 (2016) 160–165.

[56] X. Nie, F. Ma, D. Ma, K. Xu, Growth mode evolution of hafnium oxide by atomic layer deposition, J. Vac. Sci. Technol. A 32 (2014), 01A109.

[57] M. Krbal, J. Prikryl, R. Zazpe, F. Dvorak, F. Bures, J.M. Macak, 2D $MoSe_2$ structures prepared by atomic layer deposition, Phys. Status Solidi Rapid Res. Lett. 12 (2018), 1800023.

[58] E. Østreng, K.B. Gandrud, Y. Hu, O. Nilsen, H. Fjellvåg, High power nanostructured $V_2O_5$ thin film cathodes by atomic layer deposition, J. Mater. Chem. 2 (2014) 15044–15051.

[59] Y. Gogotsi, P. Simon, True performance metrics in electrochemical energy storage, Science 334 (2011) 917–918.

[60] D.K. Nandi, S. Sahoo, S. Sinha, S. Yeo, H. Kim, R.N. Bulakhe, J. Heo, J. Jin Shim, S.-H. Kim, Highly uniform atomic layer-deposited $MoS_2$@3D-Ni-foam: a novel approach to prepare an electrode for supercapacitors, ACS Appl. Mater. Interfaces 9 (2017) 40252–40264.

[61] K. Yao, Z. Xu, J. Huang, M. Ma, L. Fu, X. Shen, J. Li, M. Fu, Bundled defect-rich $MoS_2$ for a high-rate and long-life sodium-ion battery: achieving 3D diffusion of sodium ion by vacancies to improve kinetics, Small 15 (2019), 1805405.

[62] Z. Xu, K. Yao, Z. Li, L. Fu, H. Fu, J. Li, L. Cao, J. Huang, Sulfur nanodots as $MoS_2$ antiblocking agent for stable sodium ion battery anodes, J. Mater. Chem. 6 (2018) 10535–10542.